Chapter 14
Dynamic and Thermal Interactions in Metal Cutting

P. Eberhard, U. Heisel, M. Storchak, and T. Gaugele

Abstract. This contribution presents a physical cutting process model based on the Discrete Element Method (DEM), which allows the simulation of dynamic and thermal interactions in metal cutting. Core component of the approach is the DEM model of a solid with elastic-plastic deformation modes, which is verified in standardized tensile and Charpy impact tests as well as other non-standardized tests. The model is enhanced such that the thermo-dynamics of a solid due to heat conduction can be included, which is also verified in different tests. The applicability to model-cutting processes is shown in the simulation of orthogonal cutting processes. The results of the simulation are compared to experimentally obtained results for both forces as well as temperatures. For verification purposes, an FEM model is made, which predicts both forces on the tool as well as temperatures.

14.1 Introduction

For decades, there has been a steady increase of the quality of machine tools. For further improvement, a better understanding of the interactions between the machine tool and the physics of the manufacturing process is necessary. A mapping of the process to an appropriate physical model is often challenging from a computational mechanics point of view as there are often large deformations as well as a steady evolution of boundaries and new surfaces. For a mesh-based approach, this may prove to be awkward due to constant remeshing and a mapping of quantities between successive meshes. Alternatively, a meshless method like the DEM naturally includes the separation of material and large deformations. A conventional DEM model consisting of rigid spherical particles for granular material is enhanced by cohesive visco-elastic-plastic interactions. This generates a 'granular solid', which is subjected to virtual material tests to verify it and to determine parameter values. The mechanical state of the particles is extended to include thermal properties and heat conduction, too. Thereby, an established workpiece model is machined in orthogonal cutting processes. The obtained results are compared to experimentally-obtained results and FEM references. The experiments are made on a specifically designed test bed, which allows the measurement of forces on the tool during cutting. To include different cases of cutting, the stiffness of the test

B. Denkena and F. Hollmann (Eds.): Process Machine Interactions, LNPE, pp. 309–328.
springerlink.com

bed as well as the angle of inclination of the tool can be modified so oblique cutting processes can also be considered.

14.2 Experimental Investigations

For verification purposes experimental investigations are made. The following section describes the setup and the results of the experiments.

14.2.1 Test Setup

To investigate the interaction processes in cutting a test bed is set up, whose CAD model and machine prototype are shown in Figure 14.1. The bed of the test bed is manufactured from massive polymer concrete slabs und carries the tool holder, which is mounted in gantry design. In addition, the gantry is connected to the bed via solid tension rods. The pre-stressing of the tension rods is adjustable. For this reason, flexibilities can be systematically introduced in order to verify the coupling model. Moreover, a table is mounted onto the bed, which carries the tool holder via a measurement platform. The table drive is realized by a linear direct drive, which enables a continuous modification of the cutting speed from 0 to 200 *m/min* and hence covers the conventional cutting speed range. The drive system consists of a linear engine, a servo control unit including power electronics and a PC as superordinate control. An important objective in the design of the test bed is to largely disable the dynamic behavior of the structure when measuring the process forces.

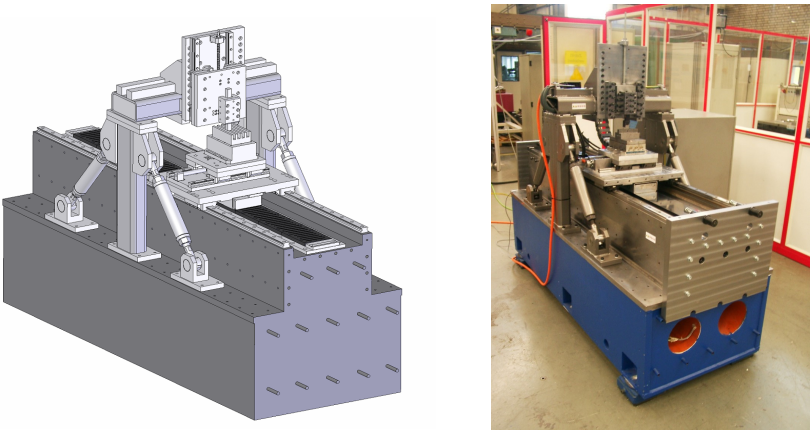

Fig. 14.1 CAD-model and general view of the test bed

To examine the stiffness of the test bed different measurements are performed in feed direction (x-axis) and in the direction of depth setting (z-axis). A stiffness of approximately 490 *N/µm* is determined in z-direction for the table and tool

holder, which represents an excellent value. The stiffness of the gantry in x-direction is 230 *N/µm*, which is also sufficient for the investigations to be conducted.

In order to investigate to what extent the stiffness of the structure is influential, flexibilities are systematically introduced into the structure by means of specifically developed stiffness elements. Thus, the stiffness between tool holder and gantry as well as between workpiece and table can be reproducibly modified. This is carried out by means of a "stiffness element", which consists of two plates with disc springs placed in-between, see Figure 14.2a. The stiffness of the elements is subsequently modified in the range from 1,000 to 10,000 *N/mm*, whereby the effect of the static stiffness, apart from the possible minor stiffness of the tool, can be relatively well distinguished from the effect of the static stiffness of the entire setup. The modification of the stiffness of the element is guaranteed by the number of disc springs. Figure 14.2b exemplifies the examination of two different static stiffnesses of the element. The diagram in Figure 14.2b suggests that the stiffness element guarantees a maximum displacement of 0.5 *mm*. If further load is applied, the element shuts and its two plates operate as one solid common body.

To investigate the effect of the static stiffness on the resultant forces and to determine the resultant forces in orthogonal and free three-dimensional cutting, a measuring chain was assembled and set up. The signals were recorded and processed as well as controlled and evaluated by means of a program developed under the LabVIEW GUI 7.1, which consists of three separately operating LabVIEW programs. One program serves to record and visualize the data, another to calibrate and another to statistically evaluate the resultant forces.

Free three-dimensional cutting is guaranteed by the twisting of the tool head around the angle of inclination λ_S. The general view of the test setup for three-dimensional cutting is shown in Fig. 14.3. In the investigations of the machining of steel C45, the angles of inclination of 15° and 45° are used and the cutting force F_x, the shear force F_y and the thrust force F_z are recorded.

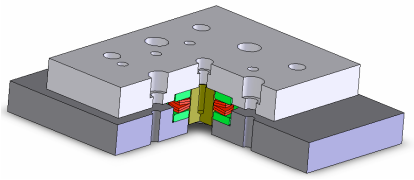

a)

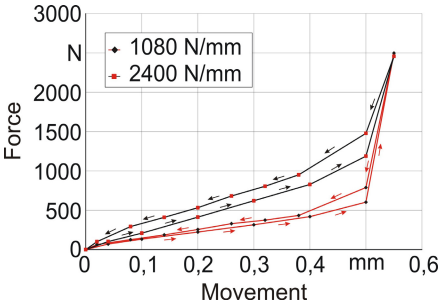

b)

Fig. 14.2 Stiffness element and its static stiffness

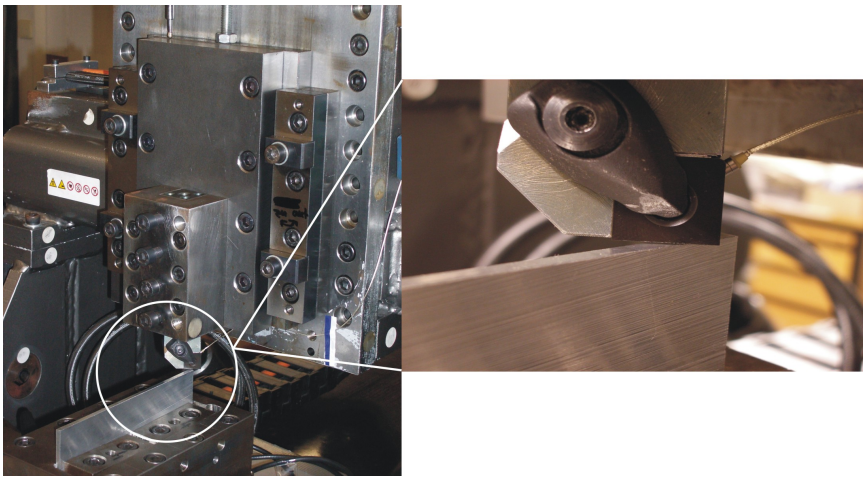

Fig. 14.3 Performing a free three-dimensional cutting process on the test bed

The heat flows are established by experimental determination of the temperature change in the parts and assemblies. To investigate the effect of the ambient temperature on the heat flows inside the machine structure, the test bed is put into a climate chamber together with the entire measuring equipment required for the test. In the course of the investigations, the ambient temperature is varied in a range from +14°C to +36°C, see [4].

The experimental investigations to determine the temperature in the primary, secondary and tertiary cutting zones are performed by means of semi-artificial thermocouples, which are based on the Seebeck effect [5], [6] and [7]. Two methods are applied. With the first method the temperature distribution in the workpiece and in the chip can be examined [8]. One thigh of the thermocouple is made of constantan wire, the other thigh of the material to be machined. Thus, a thermocouple of the type "J" is generated. With the second method, the temperature distribution at the border between wedge and chip can be examined [8]. In this case, one thigh of the thermocouple is formed by constantan foil, which is clamped in-between two carbide plates. The workpiece is used as the second thigh. The constantan foil and all the tools are isolated from the upper and lower inserts. Depending on the relative position of the upper and lower inserts to each other, and depending on the type of tool sharpening, the position of the foil can be modified relative to the wedge point. Hence, the cutting temperatures can be measured at different points, mainly in the secondary cutting zone. As is the case in the first method, a thermocouple of type "J" is also generated. The signals are recorded and processed as well as controlled and evaluated by means of a program developed under the LabVIEW GUI 7.1.

14.2.2 Temperature and Force Measurements

The following section summarizes the measurement of forces and temperatures.

14.2.2.1 Forces in Orthogonal and Free Three-Dimensional Cutting

The investigations of the resultant forces in both orthogonal and free three-dimensional cutting represent a data basis for the verification of cutting models. Figure 14.4 shows the course of the cutting and thrust force in the orthogonal machining of steel C45 with different cutting speeds from 50 to 150 *m/min* at different cutting depths. As expected, the dependencies show a significant rise of the forces with increasing cutting depths. The increase of the cutting speed, however, has only little effect on the resultant forces.

In three-dimensional cutting, the components of the resultant force, i. e. the cutting force F_x, the shear force F_y and the thrust force, increase, as expected, with increasing cutting depth, see Figure 14.5. The size of the cutting force, in contrast, hardly changes with an increasing angle of inclination λ_S. The course of the thrust force flattens with a greater angle of inclination and the same maximum values. The shear force F_y increases with an increasing angle of inclination. This reaction is intensified with increasing cutting depths a_p. The increase of the shear force with an increasing angle of inclination can be explained with the extension of the cutting length or width.

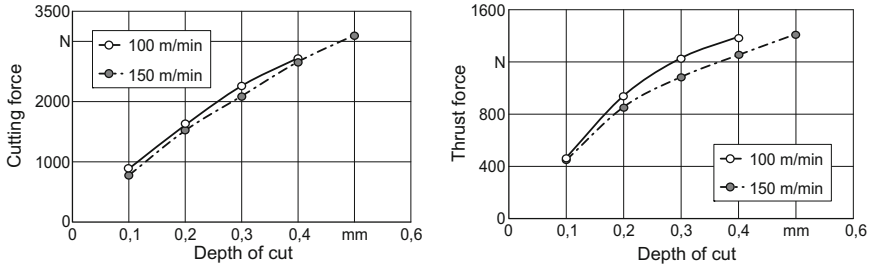

Fig. 14.4 Resultant forces in orthogonal machining of steel C45

14.2.2.1 Investigation of the Temperatures in the Cutting Zones

Moreover, investigations on thermal phenomena in the cutting zones are conducted in order to verify the cutting model. The temperatures in the primary, secondary and tertiary cutting zones and in the base material are used as references. Characteristic signals in the primary cutting zone and in the chip are shown in Figure 14.6.

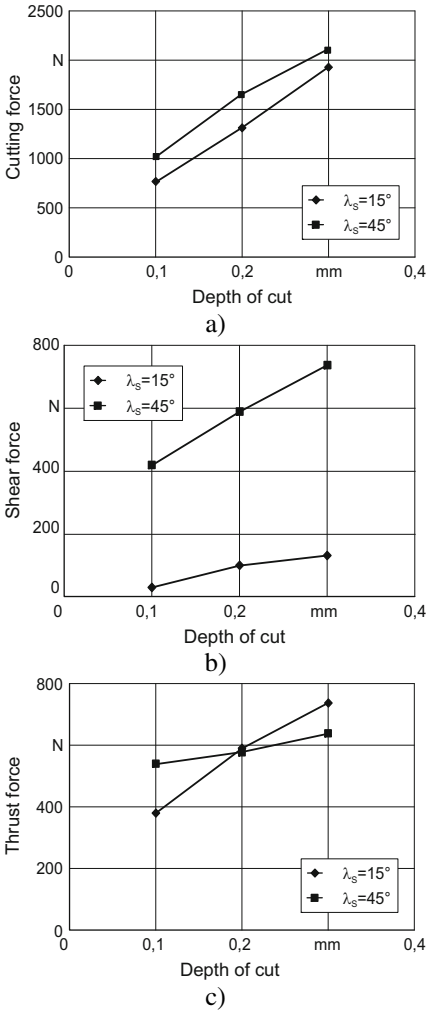

Fig. 14.5 Dependency of the resultant forces on the angle of inclination λ_S

The shape of the signal and the amplitude during cutting correspond to the position of the temperature sensor and to the constantan thigh in the different layers of the material respectively. In practice, the method with the welded constantan wire [8] can only be applied in comparably large cutting depths so as to realize a reasonable resolution and to be able to precisely determine the position of the constantan thigh. Therefore, this method was applied in experimental investigations to determine the temperature in the primary and tertiary cutting zone and in the base material. The method on the basis of the constantan foil clamped in-between two inserts does not exhibit such a restriction and was hence used as the basic method for recording the cutting temperatures in the secondary cutting zone. The change in temperature in the secondary cutting zone or in the chip, depending on the

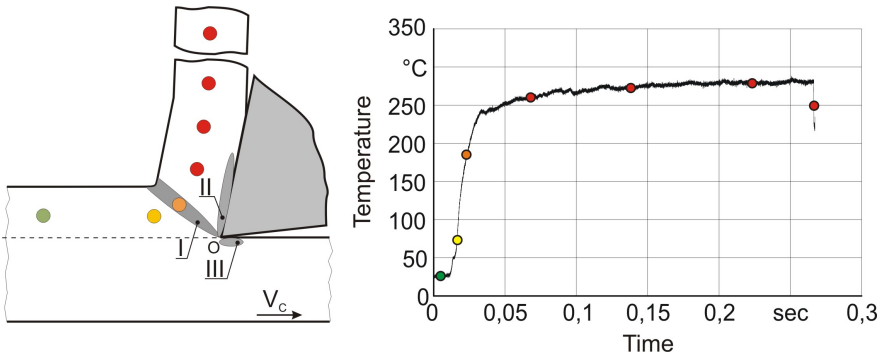

Fig. 14.6 Characteristic course of the signal in the primary cutting zone and in the chip

cutting speed and the distance *L* of the measuring point and on the position of the constantan foil relative to the cutting edge of the die plate, is shown in Figure 14.7 for a free three-dimensional cutting process. The figure shows that the change in temperature at a cutting speed of 50 *m/min* is extreme. The maximum is reached at a distance of 1 *mm* between the measuring point and the cutting edge. This corresponds to the known temperature distribution in the secondary cutting zone. At cutting speeds of 100 *m/min* and 200 *m/min*, a temperature maximum is only reached at greater distances to the cutting edge. The results of the FEM cutting model are summarized in Table 14.1 for a distance of 0.25 *mm* to the cutting edge. The maximum difference between the simulated and experimentally recorded results amounts to 13.8 %, which can be regarded as an acceptable error in thermal investigations.

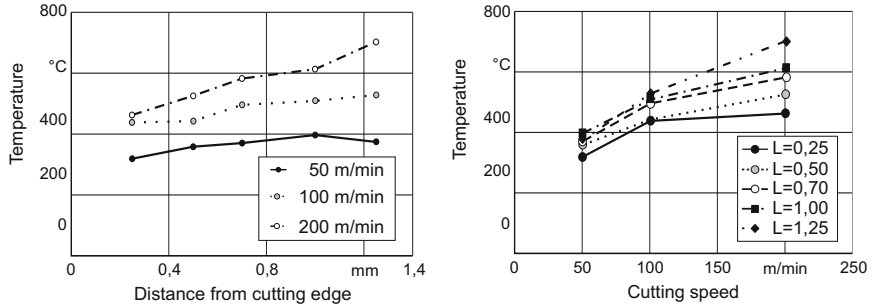

Fig. 14.7 Temperature change in the secondary cutting zone

Table 14.1 Simulated and experimentally recorded temperatures in the secondary cutting zone

v, m/s	T_{sim}, °C	T_{exp}, °C
50	370	319
100	475	438

14.3 Material and Cutting Models

Two cutting models are set up. One is based on the FEM, the other is built on a mesh-free DEM approach.

14.3.1 FEM

The FEM model was developed with the commercial product LS-DYNA for the orthogonal and three-dimensional cutting process [9], [10]. In setting up the model it is assumed that the conditions along the cutting edge are the same. A boundary condition for the workpiece is that the lower workpiece edge is to be fixed in both directions. Regarding the tool it is assumed that the edges averted from the workpiece are fixed in the direction of depth setting. The movement of the tool is predetermined by a rheonomic constraint in feed direction.

The algorithm for the plastic deformation comprises the following calculation methods:

- Initialization (initial conditions, boundary conditions, maximum integration time step size and step size for remeshing)
- Organizing the time cycle
- Calculating the clamping condition
- Evaluating the fraction criterion (Johnson-Cook criterion, geometrical criterion and criterion of maximum tensile stress. If one criterion is fulfilled for one element, the element is removed.)
- Controlling the step size to renew the FE mesh

The calculation is organized by means of the developed program manager OCFEM. The program manager has its own pre-processor to prepare the entry data, a mesh generator, the control of the LS-DYNA solver and the LS-DYNA post-processor. Furthermore, another post-processor is available to extract the diagrams of the cutting force components and of the specific chip forming work. A schematic diagram of the operating mode of the OCFEM with external modules and files is shown in Figure 14.8. The data transfer between the individual models takes place by means of ASCI files. The developed FEM model was verified by a comparison of the experimental and calculated values. The cutting and thrust forces and the chip compression coefficient K_a were used as references. Steel C45, which was cut with a cutting speed of 100 *m/min* at a depth of cut of 0.1 *mm*, was used as test material. A value of 8° was selected for the cutting angle and a value of 5° for the angle of clearance. The results of the verification of the FEM cutting model are presented in Table 14.2. The f is a chip load per revolution. The results suggest that the model provides adequate results for the cutting force but inadequate values for the thrust force and chip compression coefficient, i. e. values that are clearly too low.

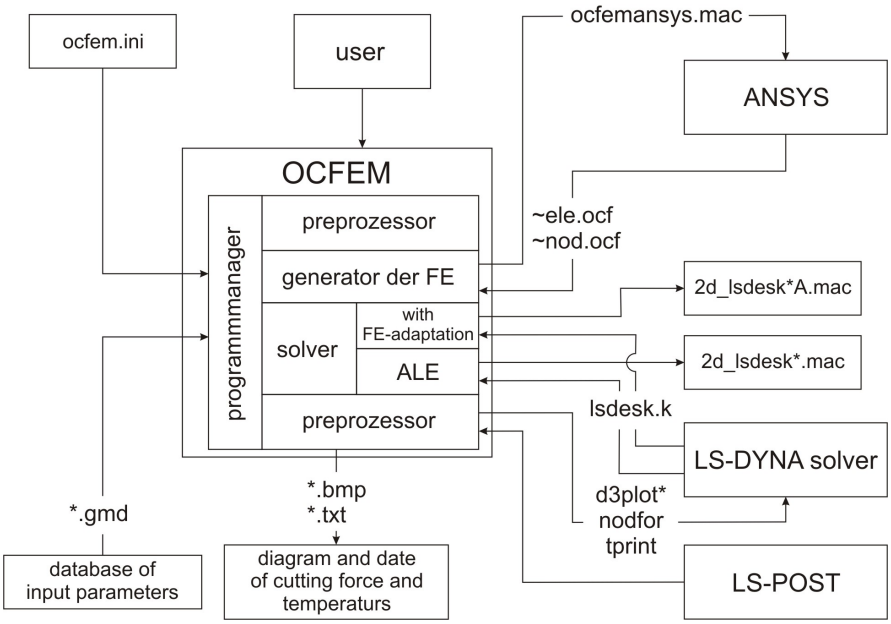

Fig. 14.8 Schematic diagram of the program setup with OCFEM

Table 14.2 Data for FEM verification

f, *mm/rev*	K_a			F_x, *N*			F_z, *N*		
	Exp.	**FEM**	**Err. %**	**Exp.**	**FEM**	**Err. %**	**Exp.**	**FEM**	**Err. %**
0.15	2.72	1.9	-30	561±45	416	26	383±37	76	80
	2.6		-27	519±36		20	334±31		77.24
	2.4		-13	558±50		4.35	369±60		47.38
0.30	2.4	1.9	-21	940±55	832	11.5	473±57	106	77.6
	2.2		-14	875±92		4.9	430±55		75.3
	2.5		-16	534±39		4.8	377±38		51.2

14.3.2 Discrete Element Method

Some fundamentals of the Discrete Element Method (DEM) are summarized in the following. This method is then used for cutting simulations.

14.3.2.1 Dynamics of Particle Systems

The DEM models the motion of usually free and rigid particles, which interact with each other, and the system boundaries in case of physical contact. A DEM algorithm can be sub-divided into three major steps, which are neighborhood search, force computation and integration of the equations of motion. The neighborhood search delivers the information as to which particles are in physical contact and can therefore interact. Based on this information, the forces acting on the particles are evaluated. Usually, a force-displacement approach is employed, which calculates penalty forces based on negligible overlaps. The last step is to integrate the equations of motion.

Neighborhood search algorithms are not explained here. For information about those and more detailed information about the method in general refer to [11].

The translational dynamics of a free particle **i** with position vector $\mathbf{r}_i$ is readily described using Newton's equation, see [12],

$$m_i \ddot{\mathbf{r}}_i = \mathbf{f}_i \tag{1}$$

with the vector of external forces $\mathbf{f}_i$. If rotational dynamics also has to be considered, Euler's equation of rigid body motion can be used, which reads

$$\mathbf{I}_i \cdot \dot{\boldsymbol{\omega}}_i + \boldsymbol{\omega}_i \times \mathbf{I}_i \cdot \boldsymbol{\omega}_i = \mathbf{t}_i \tag{2}$$

where $\mathbf{I}_i$ is the particle's inertia tensor, $\boldsymbol{\omega}_i$ is its rotational velocity and $\mathbf{t}_i$ the vector of external torques. The differential equations (1) and (2) can be solved with several numerical integration schemes. The model setup with dynamically moving particles and evolving boundaries in conjunction with impacts indicates an integrator, which is not sensitive to jumps in the right hand side of the equation. Furthermore, it should be possible to implement it in an implicit manner for stability reasons as in a general case the frequencies of the system are not known in advance for all times. For these reasons, an implicit Newmark scheme is chosen. See [11] for the details.

14.3.2.2 Particle Force Laws

The right hand side of equations (1) and (2) contains force laws, which are evaluated based on force-displacement relationships. To generate a repulsive potential, which is used, if two separate bodies collide, either linear springs are used or, limited to spherical particles, a Hertz contact force, see [13]. To define a realistic material model of engineering materials, however, cohesive forces are needed. Depending on particle shape, the physics of the problem and other factors, different approaches can be employed. In this approach, spheres are used as the only particle shape as the contact geometry is then determined fast and computationally-efficient, thus allowing for a finer discretization. The chosen approach is to connect adjacent spheres with massless, visco-elastic-plastic rods in their centroids, which generates what will be called a 'granular solid'.

The visco-elastic-plastic rods are represented by a force law, which has been developed based on a piece-wise linear hardening model in [14]. Subjecting a duc-

tile specimen to uni-axial loading generates a stress-strain relationship, as depicted in Figure 14.9. Loading beyond the yield point $\sigma_{0.2}$ causes plastic flow of the material. Analogously, the strain $\varepsilon_{0.2}$ corresponding to $\sigma_{0.2}$ can be defined. Subsequent loading in the opposite direction causes the material to flow plastically further, if $\sigma < \sigma_{y2}$ with $|\sigma_{0.2}| > |\sigma_{y2}|$. Based on this observation, the model as illustrated in Figure 14.10 is developed. The stress strain relationship is governed by

$$\sigma = E_{\text{rod}}\varepsilon_{0.2} + k(\varepsilon - \varepsilon_{0.2})\,. \tag{3}$$

A loading below $\sigma_{0.2}$ results in a linear elastic state of stress with Young's modulus E. Further loading beyond the elastic limit results in plastic flow with hardening determined by parameter k. In that case, the initial stress-strain-curve is shifted in the stress-strain-plane by the parameters σ_0 and ε_0, which are obtained by equating the lines $g(\varepsilon)$ and $h(\varepsilon)$, see [15] for a detailed explanation.

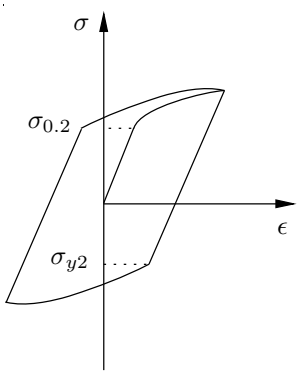

Fig. 14.9 Stress-strain hysteresis

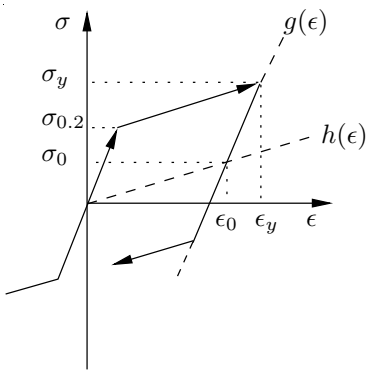

Fig. 14.10 Elastic-plastic force law

The state of stress σ_{ij} in a rod connecting two particles i and j results in a force acting on the particles it connects. The elastic plastic force $f_{i,ep}$ acting on particle i is calculated by

$$f_{i,ep} = \sum_j \sigma_{ij} A_{ij} \tag{4}$$

where A_{ij} is the cross sectional area of the rod. It is calculated as arithmetic mean of the radius of both particles involved. As each real material sustains loading only to a certain limit, the rod connection is removed, if

$$\sigma \geq \sigma_{\max} \tag{5}$$

where $\sigma_{\max}$ is the maximum bearable stress of the rod connection. This can also be expressed as maximum bearable strain $\varepsilon_{\max}$.

14.3.2.3 Mechanical Properties of the Solid

The cohesive force interaction is applied to all particles, which mechanically interact in the initial configuration. The procedure to generate an initial configuration

is roughly sub-divided in a deterministic approach and two random approaches. In the deterministic approach, the particles are arranged as a mono-disperse distribution in a regular, face-centered cubic lattice (fcc), which is a purely geometric problem. The random approaches require a full simulation each time until a static equilibrium of the system is reached. The first random approach is to drop a distribution of particles into a container under the influence of gravity and wait until they come to a rest. The second approach uses a containment holding an aggregate of particles, which is sufficiently smaller in volume than the containment. In the course of the simulation, the particles are inflated and move randomly within the box. Increasing particle radii cause increasing pressure on the box walls, which is used as a trigger to stop the simulation as soon as a pre-defined pressure threshold is reached. The random approaches can be used in a meaningful manner with poly-disperse distributions.

The generated solid is subjected to several tests to assess its mechanical properties. These are a test for isotropy, a tensile test and a Charpy impact test. For an isotropy test, specimens are subjected to slow tensile and torsional strain to examine how many particles are needed and how they should be arranged. Tensile tests are made according to the appropriate standard, which allows for comparison with experimental results and results from literature. The objective of a tensile test with regard to a granular solid is to determine parameter values for the interaction, which governs elastic-plastic behavior. For a more detailed explanation of tensile and isotropy tests and some results, see [16]. To examine how the model behaves under dynamic loading as opposed to static loading, as in the case of the tensile test, a Charpy Impact Test is conducted as specified in the corresponding standard [17]. In a Charpy impact test, a notched specimen with a square cross-section. as shown in Figure 14.11, is hit by a hammer on the opposite side of the notch, as indicated in Figure 14.12. The hammer is fixed to a pendulum and released from a pre-defined height, thus hitting the specimen with a known kinetic energy. As the specimen breaks during the impact and absorbs energy, the pendulum with the hammer reaches a smaller amplitude after impact than it had before. The amount of absorbed energy can then be readily calculated from the difference of amplitudes.

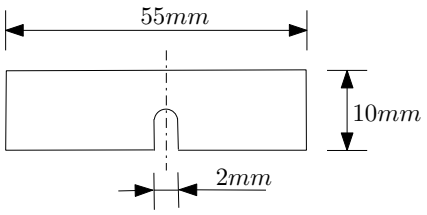

Fig. 14.11 Standardized test specimen

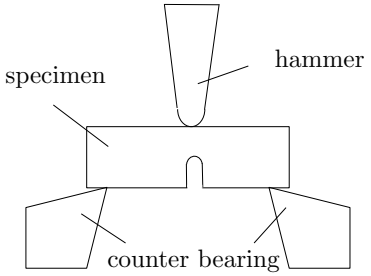

Fig. 14.12 Test setup

A Charpy impact test is simulated with a regular specimen, i. e. the particles are arranged in an fcc lattice and an inflated specimen with parameters as given in Table 14.3.

Table 14.3 Parameters of Charpy impact test specimen

	regular specimen	**inflated specimen**
particle radius r [*m*]	$4*10^{-4}$	$4*10^{-4}$
number of particles [*1*]	20000	20000
E_{rod} [N/m^2]	$5.31*10^{10}$	$11.2*10^{10}$
$E_{0.2}$ [*1*]	0.285%	0.295%
$\dot{\varepsilon}$ [*1/s*]	1.0	1.0
ρ [kg/m^3]	2700	2700

The amount of absorbed energy for both types of specimen is shown in Figures 14.13 and 14.14. Increasing the maximum strain ε_{max} before rupture for a rod increases the amount of energy it can absorb. This can be seen in Figure 14.13, where ε_{max} is chosen to be 0.07, 0.08 and 0.09. The best agreement with the experimental value of 6.99 J is found for ε_{max} = 0.08. In a similar manner, the absorbed work is determined for a random specimen as seen in Figure 14.14. Here, the best agreement is found for ε_{max} = 0.09. An alternative setup of the test is given in [18].

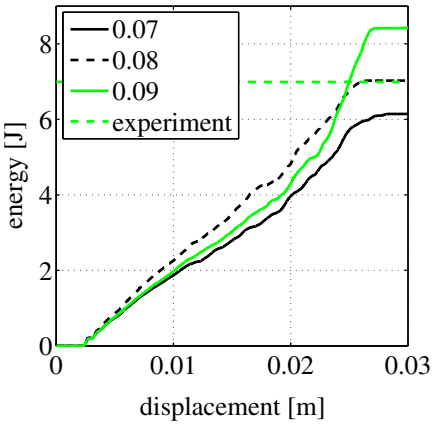

Fig. 14.13 Absorbed energy for regular specimen

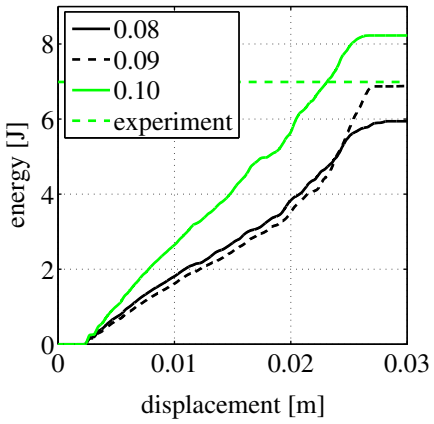

Fig. 14.14 Absorbed energy for inflated specimen

14.3.2.4 Thermal Interaction

Apart from reproducing a cutting process on a kinematic and kinetic level, thermal aspects have to be considered, too. Analogously to the mechanical state and

interactions, a thermal state and thermal interactions are defined. To each particle i with mass m_i and heat capacity c_i a temperature T_i is assigned, whose change is governed by

$$\Delta Q_i = c_i m_i \Delta T_i \tag{6}$$

where Q_i is the internal energy. A finite change of internal energy $\Delta Q_i = \Delta Q_j$ is induced, if two particles i and j interact mechanically, i. e. are in contact. The exchange of energy is governed by Fourier's law, see [19],

$$\dot{Q} = \frac{\lambda A_{ij}}{\delta_{ij}} \left(T_i - T_j \right), \tag{7}$$

and depends on the heat conductivity λ of the material, the distance of the particles δ_{ij} and the cross-section A_{ij}, which the heat flows through. For a definition of the flux surface, see [23].

14.3.2.5 Setup of the DEM Orthogonal Cutting Model

For the orthogonal cutting model, a setup as depicted in Figure 14.15 is chosen. The tool has no dynamics of its own. Constraints are used for both feed and depth of cut h. The workpiece has length l and height H.

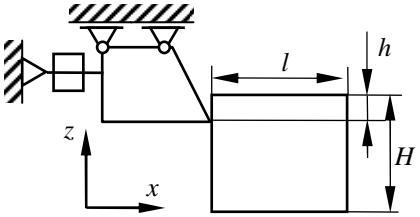

Fig. 14.15 Model setup for orthogonal DEM cutting simulation

An illustration of the model is shown in Figure 14.16.The rake angle $\alpha = 8°$ and clearance angle $\gamma = 4°$ are fixed. The tool surface is described by triangle elements interacting with the spheres of the workpiece model based on the Hertz force law, see [11]. The forces acting on each triangle element are accumulated on a common reference frame and can thus be interpreted as cutting and passive force. For the temperature interaction, all dissipative force components, e. g. plastic force components, are interpreted such that they increase the internal energy and thus the temperature. Depending on the material and the model, only a fraction $0 \leq \beta \leq 1$ of the plastic work, which is called Taylor-Quinney coefficient, causes a rise in temperature.

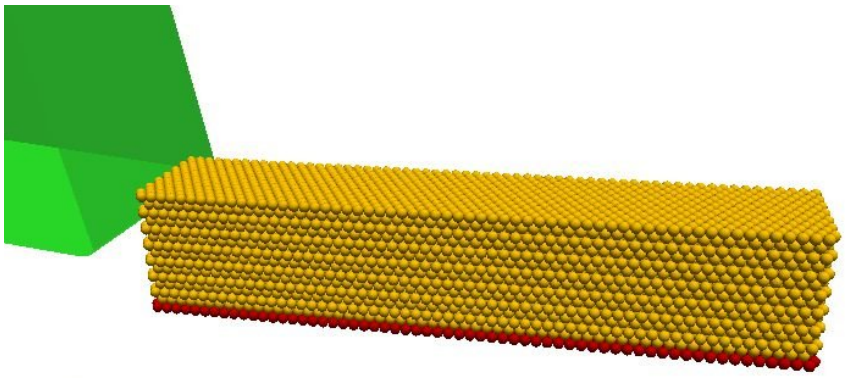

Fig. 14.16 DEM cutting model

14.3.2.6 Comparisons of the DEM Model with Experimental Results

To assess the quality of the DEM model, experimentally obtained results for both cutting forces and temperatures generated during cutting are compared with the numerical results. For the temperature interaction it is assumed that plastic deformation is dissipated with a Taylor-Quinney coefficient $\beta = 0.4$ for aluminum and $\beta = 0.9$ for steel. The parameters of the interaction are chosen as $E_{rod} = 1.8 \cdot 10^{11}\ N/m^2$, $\varepsilon_{max} = 0.16$, $\varepsilon_{0.2} = 0.003$, $k = 0.01 \cdot E_{rod}$, and $r = 0.04\ mm$. The experimental and simulated cutting forces are compared in Figure 14.17 for different depths of cut h ranging from $h = 0.2\ mm$ to $h = 0.4\ mm$.

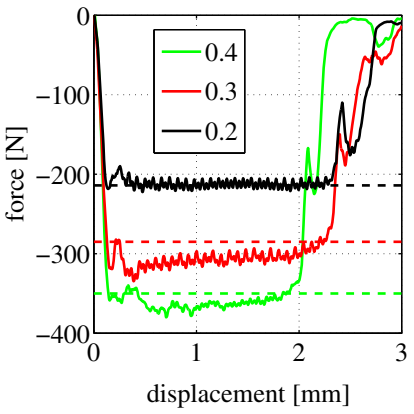

Fig. 14.17 Cutting force for Aluminum AlMgSi1.0

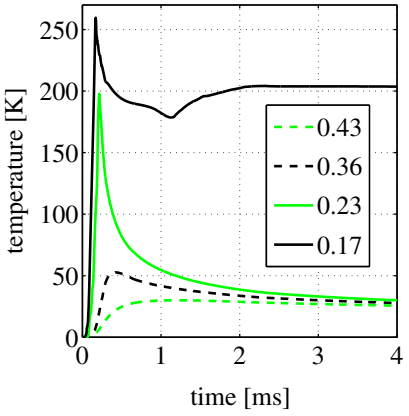

Fig. 14.18 Temperature increase for $h = 0.2$ mm

The experimental results are shown as constant levels with dashed lines and with the color-coding indicating the depth of cut. It can be seen that for $h = 0.2$ *mm* there is good agreement in the steady state regime. For larger depths of cut, agreement is slightly worse but still good. The temperature increases generated during cutting are shown in Figure 14.18 for different vertical positions measured from the top of the workpiece indicated in the legend in [mm] for $h = 0.2$ *mm*. In the chip at a depth of 0.17 *mm*, a rise of 200 K can be reported. This fits quite well to the results reported by [20]. For Ck45, the forces of the steady state regime are shown in Figure 14.19. The simulated cutting force agrees well with the experimental results, which are not available for depths of cut greater than $h = 0.3$ *mm*. The evolution of the simulated passive force, which decreases and increases again with increasing depth of cut for $0.1\ mm < h < 0.3\ mm$, is due to discretization effects. The decrease for $h \geq 0.3$ *mm* is due to the chip pressing against the rake face of the tool. The temperature increase in the workpiece for $h = 0.5$ *mm* is shown in Figure 14.20 with the vertical position of measurement indicated in the legend in [*mm*], assuming a Taylor-Quinney coefficient of $\beta = 0.9$. The measured temperature increase for a depth of cut of 0.3 *mm* is $\Delta T = 340\ K$. This is significantly lower than the simulated temperature increase in the chip, which is shown for the vertical positions 0.04 *mm* and 0.43 *mm* and is found to be around $\Delta T = 450\ K$. An explanation for this behavior is a too high value for β and too much compressive plastic deformation in the chip. For vertical positions deeper within the workpiece, far better agreement can be seen, e. g. at 0.7 *mm* and 1.0 *mm*. The temperature curve for 0.56 *mm* illustrates how the temperature peaks, when the tool passes, but the heat quickly distributes in the rest of the workpiece. See [21, [22], [23]for further results.

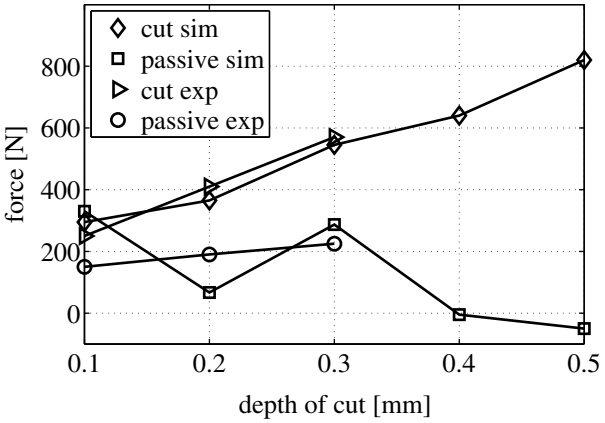

Fig. 14.19 Cutting force and passive force for Ck45

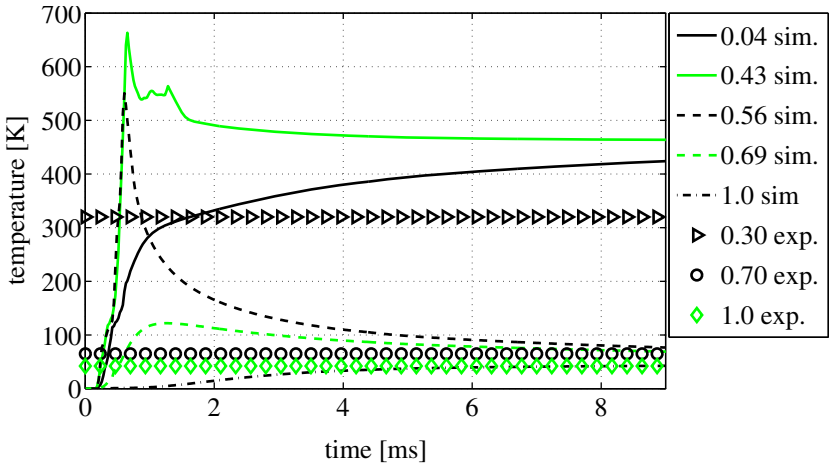

Fig. 14.20 Temperature increase for Ck45

An illustration of the cut off chip is shown in Figure 14.21. The chip is cohesive and clearly separated from the rest of the workpiece.

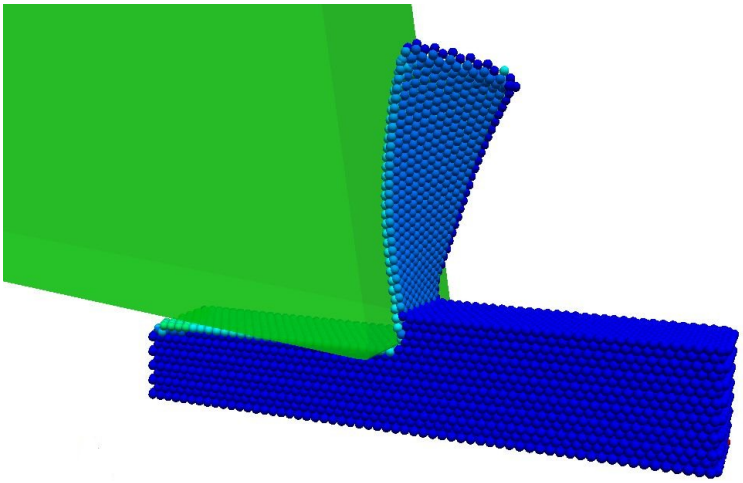

Fig. 14.21 Illustration of cut-off chip

14.3.2.7 Orthogonal Cutting with Tool Dynamics

To expand the applicability of the so-far discussed approach some constraints of the tool are removed and additional dynamics are introduced into the system. The mounting of the tool is changed giving it a rotational degree of freedom, as illustrated in Figure 14.22. This allows for a vertical movement of the tool tip and a

rotational movement of the overall tool. The tool is coupled with a rotational spring-damper combination. The dynamics of the tool is integrated into a separate simulator, a program to model multi-body systems. Both particle and multi-body simulator are coupled in a co-simulation approach, where state variables as well as kinetic quantities are exchanged at fixed time steps. See [18] for a more detailed explanation.

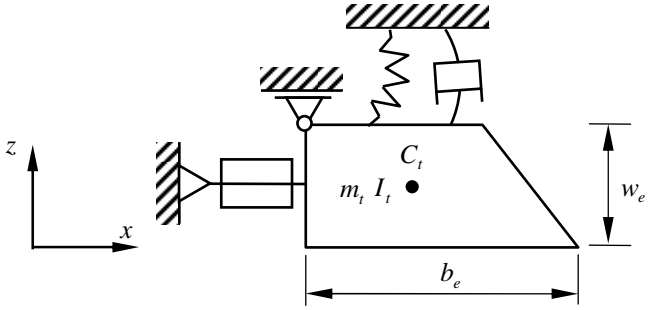

Fig. 14.22 Model setup for orthogonal DEM cutting simulation

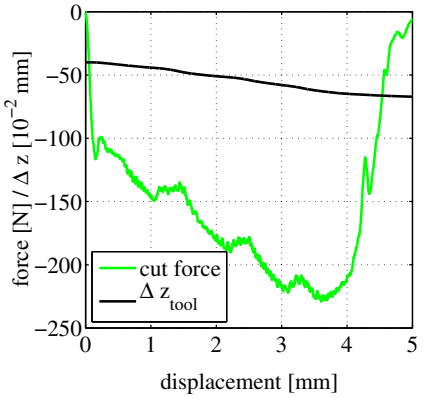

Fig. 14.23 Cutting force for elastic tool support

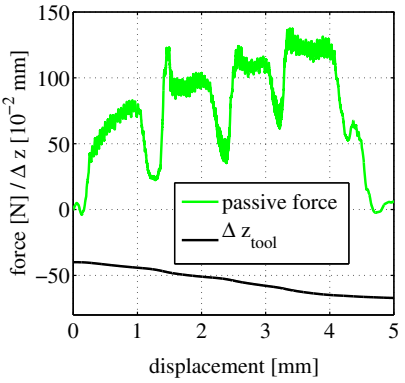

Fig. 14.24 Passive Force for elastic tool support

The model parameters are unchanged, except $E_{\text{rod}} = 5.9\ 1010\ N/m^2$. The parameters determining where the tool is fixed are chosen as $w_e = 0.02\ m$ and $b_e = 0.04\ m$, i. e. both passive and cutting force bring about a torque on the tool. The cutting force for a normalized workpiece width of 1 *mm* and the depth of cut are both shown in Figure 14.23, indicated in the legend by 'cut force' for the force and 'Δz_{tool}' for the change of vertical position of the tool tip. It can be seen that starting from an initial depth of cut of 0.4 *mm* the cutting depth continuously increases with continuous tool feed. A similar behaviour can be seen in Figure 14.24

for the passive force. A steep rise in passive force as the tool enters the workpiece is followed by a continuous increase as the cutting depth increases. The tool tip moves deeper and deeper into the workpiece due to the moment acting on the tool. As the length of the workpiece is chosen as $l = 4$ *mm* both passive and cutting force vanish for a tool displacement exceeding 4 *mm*.

14.4 Conclusion

This contribution illustrates that the proposed material model based on the Discrete Element Method allows to capture essential characteristics of elasto-plastic solids. The separation of material as shown for a Charpy impact test and in cutting processes is included without effort. The comparison of simulated and experimentally obtained cutting forces demonstrates that good agreement can be reached, both on a qualitative as well as a quantitative level. An extension of the model such that the thermodynamics of heat conduction can be included has been successfully implemented. Comparing the temperatures generated during cutting shows that, for an appropriate choice of the Taylor-Quinney coefficient, good agreement between simulation and experiment can be reached. A further enhancement of the cutting process model, such that dynamics of the tool can be included, is made based on a co-simulation approach. There, the tool dynamics is accounted for in a separate multi-body simulator. The entirely different and physically sound behavior of the system once the constraints are removed shows the increased applicability of the approach for modeling the interaction between tool, workpiece and machine.

References

[1] Tsai, L.-W.: Robot Analysis – The Mechanics of Serial and Parallel Manipulators. John Wiley & Sons, New York (1999)
[2] Merlet, J.-P.: Parallel Robots. Kluwer Academic Publishers, Dordrecht (2000)
[3] Preumont, A.: Mechatronics – Dynamics of Electromechanical and Piezoelectric Systems. Springer, Dordrecht (2006)
[4] Heisel, U., Storchak, M., Stehle, T.: Einfluss der Umgebungstemperatur beim orthogonalen Zerspanen. wt Werkstattstechnik Online 100, 89–98 (2010) (in German)
[5] Frohmüller, R., Knoche, H.-J., Lierath, F.: Aufbau und Erprobung von Temperaturmesseinrichtungen durch das IFQ im Rahmen des Schwerpunktprogramms Spanen metallischer Werkstoffe mit hoher Geschwindigkeit. Spanen metallischer Werkstoffe mit hohen Geschwindigkeiten Kolloquium des Schwerpunktprogramms der DFG, 108–115 (1999) (in German)
[6] Körtvelyessy, L.V.: Thermoelement Praxis. Vulkan Verlag, Essen (1981) (in German)
[7] Müller, B.: Thermische Analyse des Zerspanens metallischer Werkstoffe bei hohen Schnittgeschwindigkeiten. Dissertation, RWTH Aachen (2004) (in German)
[8] Heisel, U., Storchak, M., Stehle, T., Korotkih, M.: Temperaturbestimmung in den Zerspanzonen. wt Werkstattstechnik Online 100, 365–370 (2010) (in German)

[9] Heisel, U., Krivoruchko, D.V., Zaloha, V.A., Storchak, M.: Cause Analysis of Errors in FE Prediction of Orthogonal Cutting Performances. In: 10th CIRP International Workshop on Modeling of Machining Operations, pp. 141–148 (2007)
[10] Heisel, U., Kryvoruchko, D.V., Zaloha, V.A., Storchak, M., Emelyanenko, S., Selivonenko, S.N.: Finite Element Analysis of Cutting Force Dynamics. In: Proceedings of the 11th CIRP Conference on Modeling of Machining Operations, September 16-18, pp. 163–170 (2008)
[11] Fleissner, F.: Parallel Object Oriented Simulation with Lagrangian Particle Methods. Schriften aus dem Institut für Technische und Numerische Mechanik der Universität Stuttgart, Bd. 16. Shaker Verlag, Aachen (2010)
[12] Geradin, M., Rixen, D.: Mechanical Vibrations. John Wiley & Sons, Chichester (1998)
[13] Lankarani, H.M., Nikravesh, P.E.: A Contact Force Model with Hysteresis Damping for Impact Analysis of Multibody Systems. Journal of Mechanical Design 112, 369–376 (1990)
[14] Liu, K., Gao, L., Tanimura, S.: Application of Discrete Element Method in Impact Problems. JSME International Journal, Series A 47, 138–145 (2004)
[15] Fleissner, F., Gaugele, T., Eberhard, P.: Application of the Discrete Element Method in Mechanical Engineering. Multibody System Dynamics 18, 81–94 (2007)
[16] Gaugele, T., Fleissner, F., Eberhard, P.: Simulation of Material Tests using Meshfree Langrangian Particle Methods. Proceedings of the Institution of Mechanical Engineers, Part K: Journal of Multi-body Dynamics 222(K4), 327–338 (2008)
[17] DIN10045, Kerbschlagbiegeversuch nach Charpy. Deutsches Institut für Normung e.V., Berlin (1991)
[18] Gaugele, T., Eberhard, P., Storchak, M., Heisel, U.: A Discrete Material Model used in a Co-simulated Charpy Impact Test and for Heat Transfer. In: Proceedings of the 1. International Conference on Process Machine Interactions, pp. 361–369 (2008)
[19] Tychonoff, A., Samarski, A.: Differentialgleichungen der mathematischen Physik. Deutscher Verlag der Wissenschaften, Berlin (1959) (in German)
[20] Jaspers, S., Dautzenberg, J.: Material Behavior in Metal Cutting: Strains, Strain Rates, and Temperatures in Metal Cutting. Journal of Materials Processing Technology 121, 123–135 (2002)
[21] Gaugele, T.: Application of the Discrete Element Method to Model Ductile, Heat Conductive Materials. Dissertation, University of Stuttgart (2011) (submitted)
[22] Eberhard, P., Gaugele, T.: Quasi-static and dynamic properties of separable continua based on Lagrangian Particle Methods. In: Proceedings of the International Conference on Particle-Based Methods, Fundamentals and Applications (Particles 2009), pp. 398–401 (2009)
[23] Gaugele, T., Eberhard, P., Fleissner, F.: Particle Methods Used to Model Cutting Processes Including Heat Conduction. In: Proceedings of the International Conference on Particle-Based Methods, Fundamentals and Applications (Particles 2009), pp. 142–145 (2009)